Synergetic effect of multicomponent additives on limestone when assessed as a thermochemical energy storage material

Kasper T. Møller [a,b,*], Amanda Berger [a], Mark Paskevicius [a,**], Craig E. Buckley [a]

[a] Physics and Astronomy, Fuels and Energy Technology Institute, Curtin University, GPO Box U1987, Perth 6845, WA, Australia
[b] Department of Biological and Chemical Engineering, Aarhus University, Aabogade 40, Aarhus DK-8200, Denmark

ARTICLE INFO

ABSTRACT

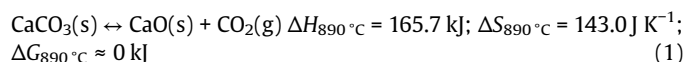The effect of adding both Al_2O_3 and ZrO_2 to limestone ($CaCO_3$) to enhance the cyclic stability and reaction kinetics of endothermic CO_2 desorption and exothermic CO_2 absorption is investigated. The formation of $CaZrO_3$ and Ca-Al-O compounds, *e.g.* $CA_5Al_6O_{14}$, is evident, which enables a substantial >80% capacity retention over 50 calcination/carbonation cycles. The additives enable fast reaction kinetics where an 80% energy storage capacity is reached within 20–30 min, which is attributed to the synergetic effect of having both Ca-Zr-O and Ca-Al-O ternary additives present. The inert nature of the formed compounds prevents sintering of the particles, whilst allowing ion migration throughout the crystal structures, catalysing the carbonation reaction.

© 2021 The Author(s). Published by Elsevier B.V.
CC_BY_4.0

1. Introduction

Energy storage remains one of the greatest challenges in the green transition due to the fluctuating nature of, *e.g.* sun and wind power production. State-of-the-art thermal energy storage is based on sensible heat in molten salts, *e.g.* a $0.4NaNO_3$-$0.6KNO_3$ mixture that operates between 290 and 565 °C, and thus relies on the specific heat capacity of the salt [1,2]. This technology is commonly found in concentrating solar power (CSP) plants, which utilises focused sun rays to heat up the molten salt and store the heat for power generation at night time when the sun no longer shines [3]. However, the low operating temperature and modest energy density (413 kJ kg^{-1} in the operating temperature interval) of molten salt technology results in relatively high energy storage cost and inspires the development of more efficient technologies with higher energy density, operating temperature to ensure a higher heat-to-power conversion efficiency based on the Carnot cycle, and lower cost [4,5]. Recently, much attention has been directed towards metal carbonates, hydroxides, oxides, and hydrides due to their high reaction enthalpies, and thus great potential for thermochemical energy

storage [3,6–8]. Calcium carbonate, $CaCO_3$, is non-toxic, widely available and thus cheap, and can operate at 890 °C with a high reaction enthalpy:

$$CaCO_3(s) \leftrightarrow CaO(s) + CO_2(g) \ \Delta H_{890\,°C} = 165.7 \text{ kJ}; \ \Delta S_{890\,°C} = 143.0 \text{ J K}^{-1}; \ \Delta G_{890\,°C} \approx 0 \text{ kJ} \quad (1)$$

Energy storage, *e.g.* in connection with a CSP plant, would involve the endothermic decomposition of $CaCO_3$ into CaO and CO_2 to take place when surplus energy is available, whereas thermal energy production through the exothermic regeneration of $CaCO_3$ would take place when energy is needed. Keeping the operational temperature around 890 °C ensures a high heat-to-power conversion efficiency ($\eta_{theoretical} \sim 74\%$) and allows low-pressure gaseous operation as the equilibrium pressure of CO_2 is 1 bar, see reaction scheme 1. However, a significant energy capacity loss in pristine $CaCO_3$ over multiple reaction cycles inhibits its utilisation as an energy storage material [9,10].

Generally, metal carbonates such as $CaCO_3$, $MgCO_3$, and $CaMg(CO_3)_2$ have proven difficult to re-carbonate once calcined [11,12]. Multiple studies have suggested ways of circumventing this inherent property, *e.g.* the addition of a molten salt, which promotes CO_2 uptake [4,13], addition of an inert material such as MgO to prevent sintering of particles [14], or by altering the reaction pathway and thus the thermodynamics of the metal carbonate formation through the addition of a metal orthosilicate [15,16]. However, an acceptable CO_2 capacity retention over multiple cycles, *i.e.* >80%, has rarely been
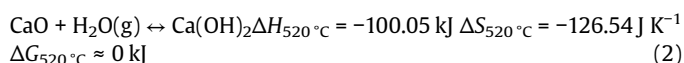
* Corresponding author at: Physics and Astronomy, Fuels and Energy Technology Institute, Curtin University, GPO Box U1987, Perth 6845, WA, Australia.
** Corresponding author.
E-mail addresses: ktm@bce.au.dk (K.T. Møller),
mark.paskevicius@curtin.edu.au (M. Paskevicius).

achieved [4,13–16]. In fact, only a few studies have achieved a steady energy capacity retention (~99%), *i.e.* in hydrothermally synthesised Ca-Al-CO$_3$ and Ca-Fe-CO$_3$ composites utilising moderate temperatures and pressures in a thermogravimetric analysis (TGA) setup [17,18]. However, the study on Ca-Al-CO$_3$ confirms that the material behaves differently in a fixed-bed reactor compared to the TGA as a significant decrease in energy capacity retention to 76% was observed after 10 cycles [18]. Finally, slow reaction kinetics are also a persistent issue with the metal carbonates and they are often debated to have two regimes, *i.e.* kinetic and diffusion controlled [19].

A steam reactivation process can be used to replenish the cyclic CO$_2$ storage capacity in CaCO$_3$ through the temporary formation of Ca(OH)$_2$, which can favourably alter the particle morphology [20]. The effect is strongly dependent on temperature and steam content, and must be performed every thermochemical energy storage cycle to maintain an acceptable cyclic capacity [20]. Unfortunately, steam reactivation must be performed at low temperature, usually below 560 °C [21], due to the thermodynamics for Ca(OH)$_2$ formation [22]:

$$CaO + H_2O(g) \leftrightarrow Ca(OH)_2 \quad \Delta H_{520\,°C} = -100.05\ kJ\ \Delta S_{520\,°C} = -126.54\ J\ K^{-1}$$
$$\Delta G_{520\,°C} \approx 0\ kJ \tag{2}$$

however, reactivation of the material after each cycle is energetically unfavourable, and thus not suitable for the operation of a CSP plant.

Recently, the authors highlighted the important properties of different additives to the CaCO$_3$ thermochemical system, which can enable highly reversible CO$_2$ release and absorption and also modify the reaction kinetics [23,34]. Hence, a CaCO$_3$-ZrO$_2$(40 wt%) composite showed improved stability whereas a CaCO$_3$-Al$_2$O$_3$(20 wt%) composite was able to achieve an energy capacity retention up to 90% over 500 cycles in a fixed-bed reactor setup [23]. Here, the synergetic effect of adding both ZrO$_2$ and Al$_2$O$_3$ to CaCO$_3$ is investigated as a multicomponent catalytic additive.

2. Experimental

2.1. Sample preparation

Two mixtures of CaCO$_3$ (Sigma-Aldrich, >99.0%, 25–50 µm) - Al$_2$O$_3$ (nanopowder, 13 nm (TEM), 99.8% purity; 20 wt%, *i.e.* ~4 g CaCO$_3$ and ~1 g Al$_2$O$_3$) and CaCO$_3$-ZrO$_2$ (Sigma-Aldrich, nanopowder, <100 nm; 40 wt%, *i.e.* ~3 g CaCO$_3$ and ~2 g ZrO$_2$) were made by adding 10 mL of ethanol (CH$_3$CH$_2$OH) to each mixture, and then ball-mill them separately in stainless steel vials for 2 h (15 min milling x 1 min pause x 8 reps; 12 × 8 mm stainless steel balls). After ball milling, the mixtures were placed in an oven at 105 °C for approximately 1 h to obtain dry powders. Finally, the two mixtures were hand ground together in a 2:1 ratio (Al$_2$O$_3$:ZrO$_2$ sample; 0.8 and 0.4 g, respectively) to produce 1.2 g of CaCO$_3$-Al$_2$O$_3$(13.3 wt %)-ZrO$_2$(13.3 wt%) sample (denoted Ca-Al-Zr, ~10 µm, see SEM section).

2.2. Thermogravimetric and differential scanning calorimetry analysis

Thermogravimetric and simultaneous differential scanning calorimetry (TG-DSC) analysis was performed on a Mettler Toledo DSC 1 instrument. The CaCO$_3$-Al$_2$O$_3$(13.3 wt%)-ZrO$_2$(13.3 wt%) sample was heated from room temperature to 1000 °C ($\Delta T/\Delta t = 10\ °C\ min^{-1}$) under an argon flow (20 mL min^{-1}) in an alumina crucible.

2.3. Sieverts experiments

The CaCO$_3$-Al$_2$O$_3$(13.3 wt%)-ZrO$_2$(13.3 wt%) sample (0.2979 g) was loaded into a SiC sample cell, which was attached *via* Swagelok parts to a custom-made manometric Sieverts apparatus [24]. The sample was heated to ~ 900 °C ($\Delta T/\Delta t = 5\ °C\ min^{-1}$) at $p(CO_2) = 10^{-2}$ bar, thus decomposing the sample. Subsequently, cycling of the sample was initiated at isothermal conditions (~ 900 °C) with carbonation at $p_{average,carbonation}(CO_2)$ ~ 5.2 bar (±0.4 bar) for 30 min in a 58.2 cm^3 volume, followed by calcination at $p_{average,calcination}(CO_2)$ ~ 0.7 bar (±0.05 bar) for 30 min in a 208.5 cm^3 volume. A total of 50 cycles of isothermal CO$_2$ absorption and desorption were collected. Finally, the sample was carbonated and cooled to room temperature under $p(CO_2)$ ~ 5 bar.

The data have been scaled according to reaction (3) and (4) occurring, leaving a 40.7 wt% CaCO$_3$ quantity, which is the active component:

$$CaO(s) + ZrO_2(s) \rightarrow CaZrO_3(s) \tag{3}$$

$$5CaO(s) + 3Al_2O_3(s) \rightarrow Ca_5Al_6O_{14}(s) \tag{4}$$
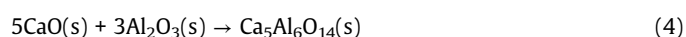
Thus, the fractional capacity in Figs. 2 and 3 is scaled accordingly and are based on 1 mol of CO$_2$ being released/absorbed according to reaction scheme 1.

The obtained data on CaCO$_3$-Al$_2$O$_3$(13.3 wt%)-ZrO$_2$(13.3 wt%) is compared to data from reference [23] on CaCO$_3$-ZrO$_2$ (20 wt%) and CaCO$_3$-Al$_2$O$_3$ (20 wt%), which were collected under similar conditions in a Hy-Energy PCTpro E&E [24]: Samples were heated to ~ 900 °C ($\Delta T/\Delta t = 5\ °C\ min^{-1}$) at $p(CO_2) = 10^{-2}$ bar, hence decomposing the sample. Subsequently, cycling of the sample was initiated at isothermal conditions (~900 °C) with carbonation at $p_{average,carbonation}(CO_2)$ ~ 6 bar (±0.5 bar) for 30 min in a 46.3 cm^3 volume, followed by calcination at $p_{average,calcination}(CO_2)$ ~ 0.8 bar (±0.1 bar) for 20 min in a 206.7 cm^3 volume. The data here were also corrected according to reaction schemes (3) and (4) depending on sample content.

2.4. Powder X-ray diffraction

In-house powder X-ray diffraction (XRD) was performed on a Bruker D8 Advance diffractometer equipped with a CuKα$_{1,2}$ source in flat-plate geometry mode. Data were collected using a Lynxeye PSD detector in the 2Θ-range 15–60° in steps of 0.02°. Rietveld analysis was performed in Topas (Bruker) and crystallite sizes were determined by the integral breadth based volume-weighted column heights (LVol-IB).

2.5. In situ synchrotron radiation powder X-ray diffraction

In situ time-resolved Synchrotron Radiation Powder X-ray Diffraction (SR XRD) data were collected at the Powder Diffraction beamline at the Australian Synchrotron, Melbourne, Australia on a Mythen microstrip detector at $\lambda = 0.825018$ Å [25,26]. The powdered sample was loaded into a quartz capillary (i.d. = 0.5 mm, o.d. = 0.6 mm), which was attached to a gas system enabling control of CO$_2$ pressure. The sample was inserted into a hot air-blower operating at 917 °C while oscillating during data acquisition. After five CO$_2$ cycles, the sample was cooled to room temperature at $\Delta T/\Delta t = 50\ °C\ min^{-1}$ under $p(CO_2) = 5$ bar. Temperature calibrations were performed using the well-known thermal expansion of NaCl and Ag [27,28].

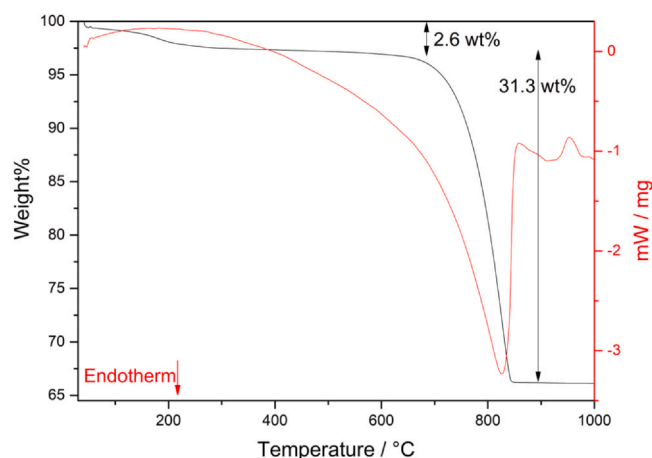**Fig. 1.** Thermogravimetric analysis and differential scanning calorimetry (TGA-DSC) of CaCO$_3$-ZrO$_2$(13.3 wt%)-Al$_2$O$_3$(13.3 wt%) from room temperature to 1000 °C ($\Delta T/\Delta t$ = 10 °C min^{-1}) under argon flow (20 mL min^{-1}).

Fig. 2. Isothermal calcination/carbonation data of the CaCO$_3$-ZrO$_2$(13.3 wt%)-Al$_2$O$_3$(13.3 wt%) over 50 CO$_2$ cycles at T ~ 900 °C and $p_{carbonation}$ ~ 5.2 bar and $p_{calcination}$ ~ 0.75 bar for 20 and 30 min, respectively. 1 mol CO$_2$ = 100% theoretical capacity, which is calculated from reaction scheme (3) and (4) as 40.7% CaCO$_3$ is the active portion of the sample.

2.6. Scanning electron microscopy

Scanning electron microscopy (SEM) and energy dispersive spectroscopy (EDS) were performed on a Tescan Mira3 FESEM coupled with an Oxford Instruments X-Max SDD X-ray detector and AZtec software. SEM images were collected using a backscattered electron (BSE) detector, an accelerating voltage of 20 kV, an aperture size of 30 µm, and a working distance of ~15 mm. SEM samples were prepared by placing powder onto double-sided conductive carbon tape on a 12.6 mm aluminium sample mount. Excess powder was removed by passing a light flow of argon gas over the sample. Samples were then sputter-coated with a 3 nm thick platinum layer before imaging.

2.7. Small-angle X-ray scattering

Small angle X-ray scattering (SAXS) data were collected on a Bruker Nanostar instrument equipped with an Excillium MetalJet source (GaK$_\alpha$, λ = 1.3402 Å). Sample powders were pressed between polymer films in transmission geometry and measured under vacuum. Data were background subtracted and put onto an absolute scale using a NIST SRM3600 glassy carbon standard [29]. Specific surface area (SSA) was calculated from the high-q Porod region (power law slope = −4) using the Unified model in the Irena software package for Igor Pro (WaveMetrics) [30,31]. This is calculated through:

$$SSA = \frac{B}{2\pi\delta\Delta\rho^2} \tag{5}$$

where B is Porod's constant refined in the Unified fit, δ is the crystallographic density, and $\Delta\rho^2$ is the scattering contrast between the powder (density of 3.05 g/cm^3, linear attenuation coefficient of 223 cm^{-1}) and vacuum.

3. Results and discussion

3.1. Thermal analysis

Thermal analysis of as-prepared Ca-Al-Zr sample reveals a small mass loss (2.6 wt%, see Fig. 1) between room temperature and 250 °C, which is assigned to evaporation of moisture from the sample, as no reacti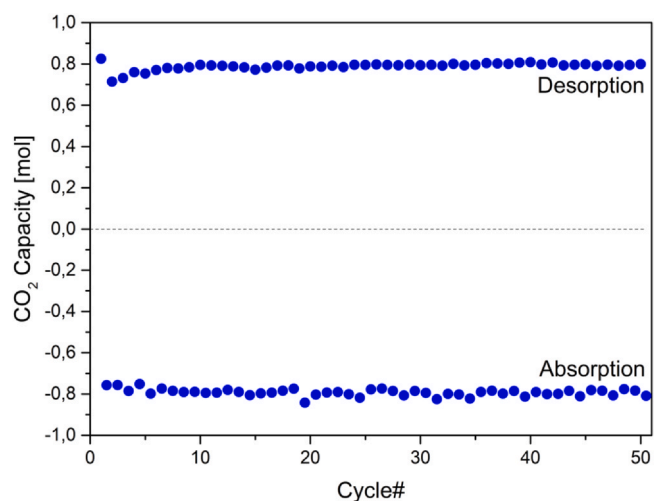on is expected in this temperature range. At ~650 °C, a one-step endothermic decomposition initiates with a total mass loss of 31.3 wt% completed by ~850 °C, which is close to the theoretical mass loss expected due to CO$_2$ release (32.2 wt%). The observed decomposition temperature is typical for CaCO$_3$ and further reactions with ZrO$_2$ and Al$_2$O$_3$ occur with the decomposition product, CaO (reaction scheme 3 and 4), without further mass loss [19,23].

3.2. Thermochemical CO$_2$ pressure cycling

The Ca-Al-Zr sample has a minor initial drop in the expected CO$_2$ capacity between the first and second cycle (from 82.5% to 71.4%, see Fig. 2). However, the system recovers and shows promise by stabilising at 80% capacity and maintaining it throughout the remaining cycles. Hence, the system is superior to a range of previously reported binary systems as also mentioned in the introduction [32]. The cyclic capacity after 50 cycles is ~81% (see Fig. 3, bottom) for Ca-Al-Zr compared to ~78 and ~68% for the CaCO$_3$-Al$_2$O$_3$(20 wt%) and CaCO$_3$-ZrO$_2$(20 wt%) samples, respectively [23]. The full thermochemical capacity (*i.e.* 1 mol of CO$_2$) is calculated based on the initial amount of CaCO$_3$ and assuming that the additives fully react with the CaCO$_3$ (reaction 3 and 4), where the cyclable CaCO$_3$ content reaches 40.7 wt% of the initial sample mass. The thermochemical system shows rapid reaction kinetics as the 80% capacity is charged/discharged within 30/20 min, respectively. Fig. 3 compares the reaction kinetics of pristine CaCO$_3$, CaCO$_3$-Al$_2$O$_3$ (20 wt%), and CaCO$_3$-ZrO$_2$ (20 wt%), along with the Ca-Al-Zr sample [23]. The ternary Ca-Al-Zr system shows rapid absorption kinetics throughout all 50 cycles. In particular, the CO$_2$ desorption kinetics in the ternary Ca-Al-Zr system become superior to the other systems as cycling increases, overcoming a previous kinetic degradation issue observed in the binary systems. This is further highlighted in Fig. 3 (bottom), which show that >90% of the absorption is completed within 5 min in all the samples, whereas the major difference between the samples is observed in the final desorption.
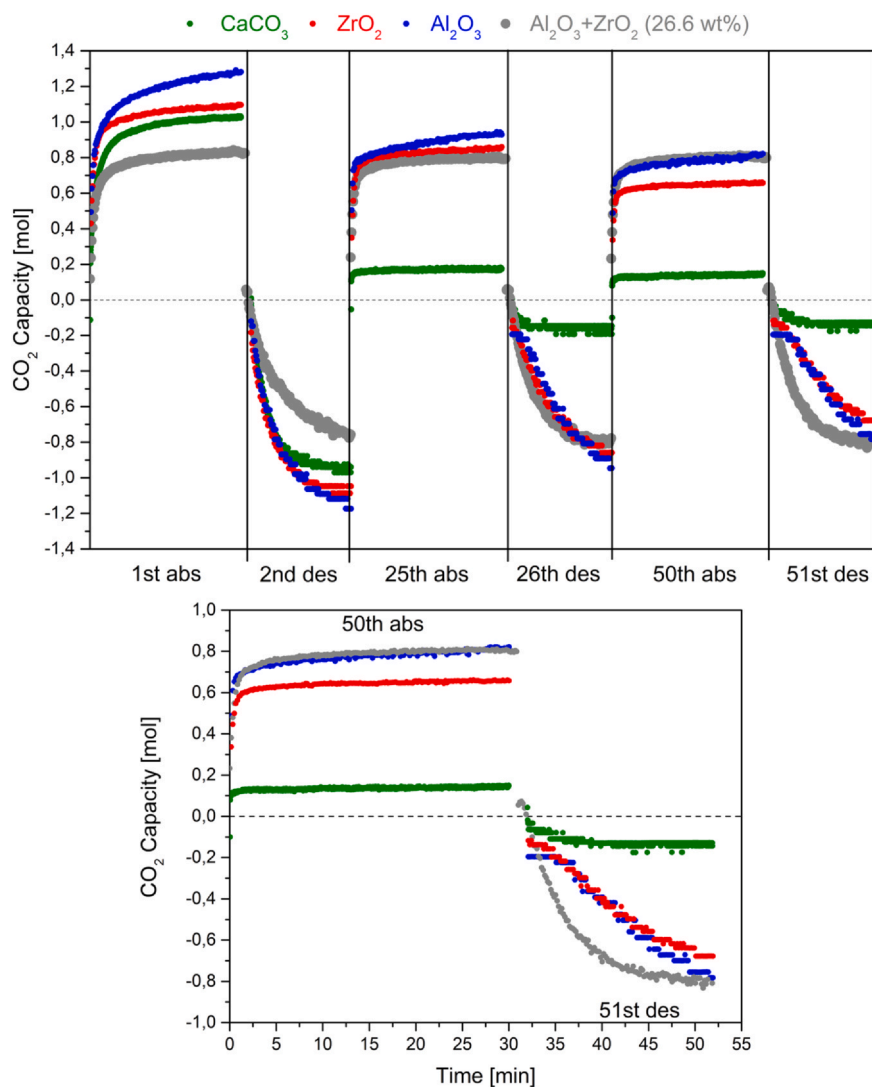
Fig. 3. *Top:* Comparison of reaction kinetics between pristine $CaCO_3$ (green), $CaCO_3$-ZrO_2 (20 wt%, red), $CaCO_3$-Al_2O_3 (20 wt%, blue) [23], and the combined $CaCO_3$-ZrO_2(13.3 wt %)-Al_2O_3(13.3 wt%). The calcination/carbonation (des/abs) cycle number is given on the *x*-axis. *Bottom:* highlighting the 50th absorption and desorption cycle. t_{abs} = 30 min, p_{abs} ~ 5–6 bar, t_{des} = 20 min, p_{des} ~ 0.7 – 0.8 bar at T ~ 900 °C. The data has been corrected according to reaction schemes (3) and (4) taking place. The capacity exceeding 1 mol of CO_2 indicates that the initial reactions (3) and (4) are incomplete at this stage.

3.3. Composition

The composition of Ca-Al-Zr after 50 cycles (in the desorbed state) was identified by XRD (see Fig. 4 and Table 1). The diffraction pattern reveals that $CaCO_3$ is present, which is assigned to partial CO_2 absorption during cooling of the sample. Furthermore, the decomposition product CaO is present along with the expected reaction products $CaZrO_3$ and $Ca_5Al_6O_{14}$ but also by-products $Ca_3Al_2O_6$ and $Ca_9Al_6O_{18}$. The compounds $Ca_3Al_2O_6$ and $Ca_5Al_6O_{14}$ are intermediates on the pathway to form Mayenite, *i.e.* $Ca_{12}Al_{14}O_{33}$, which is also identified in the sample [33]. The decrease in capacity, *i.e.* to the retained 80% over 50 cycles, may be assigned to the side reaction producing Mayenite (and partially $Ca_9Al_6O_{18}$), which was only

observed in a limited amount in a previous study with better capacity retention [23].

The *in situ* SR XRD data (Fig. 5) initially shows the rapid formation of CaO at 917 °C, which indicates the decomposition of $CaCO_3$ under 1 bar of CO_2 pressure. The reaction can be observed most significantly by intensity increases/decreases for the CaO Bragg reflections as a function of the CO_2 pressure change, although, small alterations in the intensity of the Bragg reflection from $CaCO_3$ at 2θ = 19.05° are also visible. Hence, CaO Bragg reflections quickly appear/disappear when CO_2 pressure is released/applied. Furthermore, the gradual but continuous formation of $CaZrO_3$ throughout the experiment is also evident in parallel with several Ca-Al-O compounds being observed, *i.e.* $CaAl_2O_4$, $Ca_3Al_2O_6$, $Ca_5Al_6O_{14}$, and
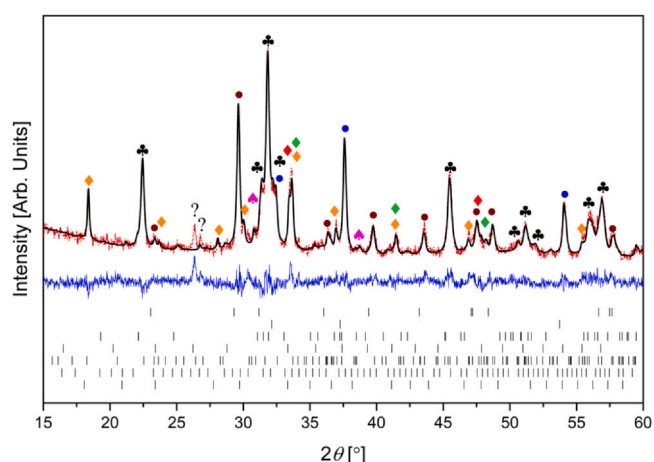
Fig. 4. Powder X-ray diffraction data of the CaCO$_3$-Al$_2$O$_3$(13.3 wt%)-ZrO$_2$(13.3 wt%) samples after 50 CO$_2$ cycles in the desorbed state. Markers: CaCO$_3$ (brown dot); CaO (blue dot); CaZrO$_3$ (clover); Ca$_3$Al$_2$O$_6$ (green diamond); Ca$_5$Al$_6$O$_{14}$ (purple spade); Ca$_9$Al$_6$O$_{18}$ (red diamond); Ca$_{12}$Al$_{14}$O$_{33}$ (Mayenite, orange diamond); unknown (question mark). Rietveld refinement of the Powder X-ray diffraction data. Y_{obs}: red; Y_{calc}: black, and Y_{diff}: blue. *hkl* Markers from the top to bottom: CaCO$_3$ (top), CaO, CaZrO$_3$, Ca$_3$Al$_2$O$_6$, Ca$_5$Al$_6$O$_{14}$, Ca$_9$Al$_6$O$_{18}$, and Ca$_{12}$Al$_{14}$O$_{33}$ (bottom). R_{wp}~9.17%.

Table 1
Sample composition extracted from Rietveld refinement after 50 CO$_2$ cycles in the desorbed state.

Compound	Weight fraction (%)	Crystallite size (nm)
CaCO$_3$	26.5(5)	30 ± 1
CaO	13.1(3)	35 ± 1
CaZrO$_3$	28.9(4)	23.2 ± 0.5
Ca$_5$Al$_6$O$_{14}$	7.0(7)	50 ± 10
Ca$_3$Al$_2$O$_6$	4.3(6)	30 ± 10
Ca$_9$Al$_6$O$_{18}$	6.8(6)	41 ± 6
Ca$_{12}$Al$_{14}$O$_{33}$	13.3(5)	44 ± 4

Ca$_{12}$Al$_{14}$O$_{33}$. Mayenite, Ca$_{12}$Al$_{14}$O$_{33}$, seems to be formed in a large fraction, which may be due to the difference in temperature between the synchrotron measurements and the cycling measurements, 917 *vs.* 900 °C, respectively, which may influence thermodynamics and/ or reaction kinetics of its formation.

4. Morphology and specific surface area

The morphology of the Ca-Al-Zr sample before and after cycling is evaluated through scanning electron microscopy (SEM), see Fig. 6. From the EDS mapping it is evident that the as-prepared sample has calcium and aluminium finely dispersed throughout. However, large particles containing zirconium, *i.e.* ZrO$_2$ (~4–10 µm) are present, likely due to its resistance to comminution given its extreme hardness. The morphology does not change significantly after cycling,
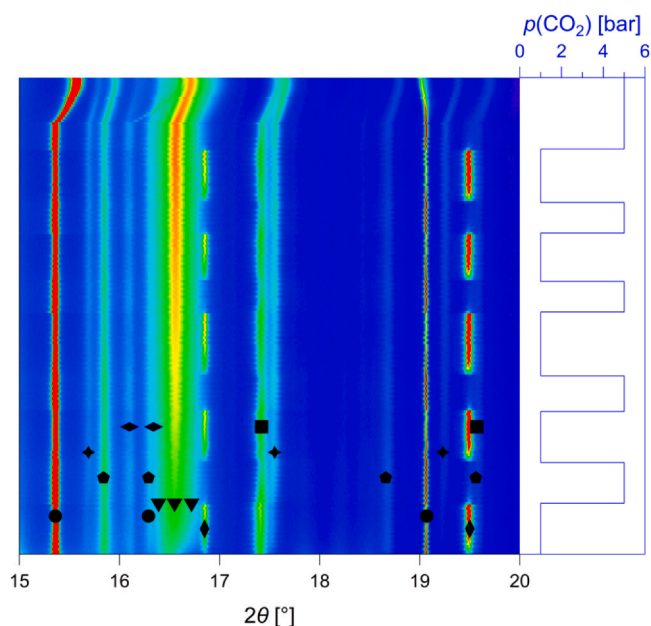

Fig. 5. *In situ* SR XRD data (λ = 0.82502 Å) of CaCO$_3$-Al$_2$O$_3$(13.3 wt%)-ZrO$_2$(13.3 wt%) at T = 917 °C. Time proceeds from the bottom to the top. The pressure profile is indicated to the right of the figure. Carbonation was performed for ~ 20 min and calcination for ~ 30 min in a total of 5 cycles. Intensity is indicated as blue: low and red: high. Markers: CaCO$_3$ (circle); CaZrO$_3$ (triangle); CaO (diamond); CaAl$_2$O$_4$ (pentagon); Ca$_3$Al$_2$O$_6$ (square); Ca$_5$Al$_6$O$_{14}$ (horizontal diamond): Ca$_{12}$Al$_{14}$O$_{33}$ (star).

although, elemental zirconium is more dispersed, which is assigned to the formation of CaZrO$_3$ rather than ZrO$_2$. This finding also matches XRD results, where ZrO$_2$ is absent after cycling, hence large Zr-rich particles (6–10 µm) must be CaZrO$_3$. Calcium and aluminium is still finely dispersed throughout the entire sample, which agrees with the observed formation of Ca-Al-O compounds. The multicomponent Ca-Al-Zr proves to have a very different morphology to CaCO$_3$ samples containing only one of the additives, *i.e.* CaCO$_3$-Al$_2$O$_3$ (20 wt%) and CaCO$_3$-ZrO$_2$ (40 wt%) [23]. The binary systems form an interconnected molten-like morphology after cycling with some degree of porosity, which is not observed for the ternary mixture.

Comparison of the specific surface areas measured by SAXS (data presented in Fig. 7) indicates the large influence of the porous ZrO$_2$ added in the as-prepared samples, as the ternary sample has a much larger surface area than the as-milled CaCO$_3$-Al$_2$O$_3$(20 wt%) sample, but similar to the CaCO$_3$-ZrO$_2$(40 wt%) sample. Despite the observations by SEM, where the ternary Ca-Al-Zr system seem to lack porosity in comparison with the CaCO$_3$-Al$_2$O$_3$(20 wt%) and CaCO$_3$-ZrO$_2$(40 wt%), the SAXS data for the ternary system shows that the surface area is approximately 2 – 6 times larger after cycling compared to the binary samples, see Table 2. The increased surface area may play a key role in the observed higher cyclic CO$_2$ capacity retention, allowing CO$_2$ to be released and absorbed from a significantly greater portion of the material more easily.
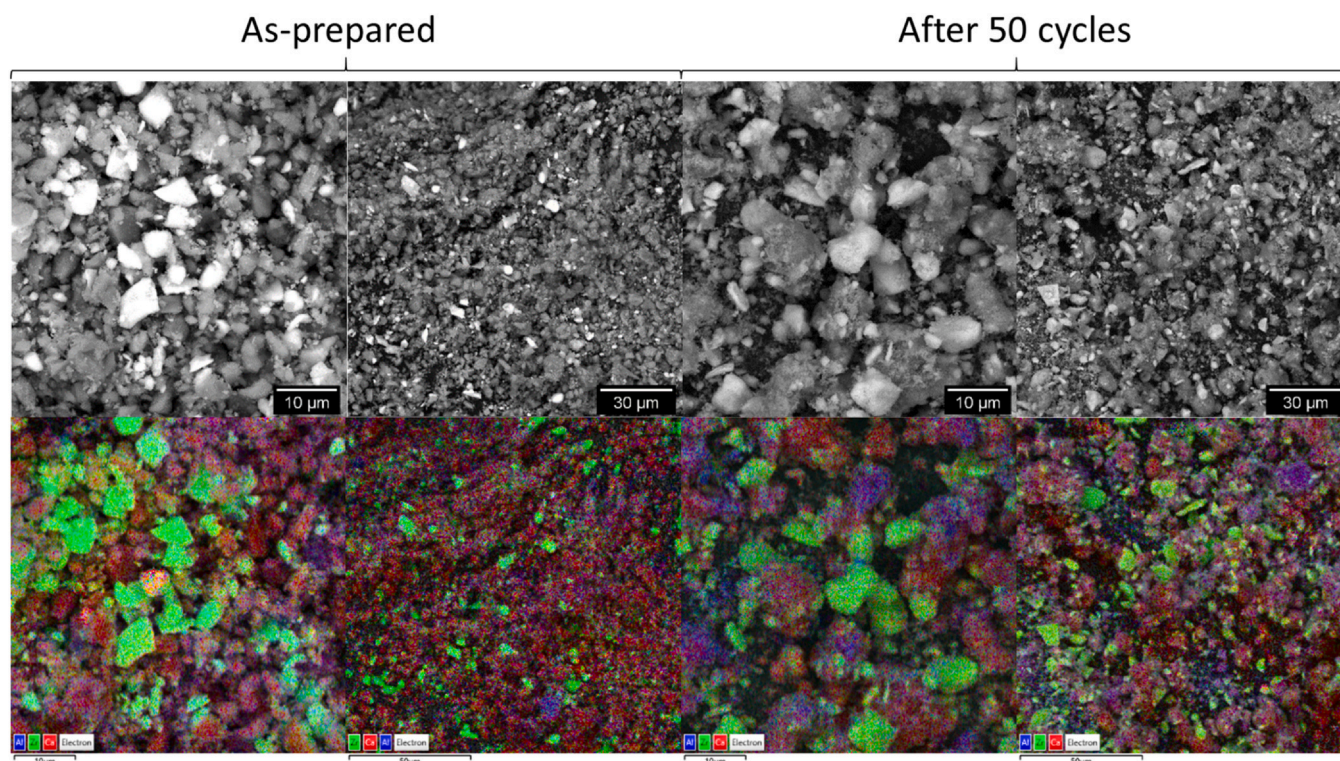
Fig. 6. Scanning electron microscopy (SEM) pictures and energy-dispersive X-ray spectroscopy (EDS) mapping of as-prepared $CaCO_3$-Al_2O_3(13.3 wt%)-ZrO_2(13.3 wt%) and after 50 CO_2 capacity cycles. EDS mapping colour code: Al: blue; Zr: green; Ca: red.
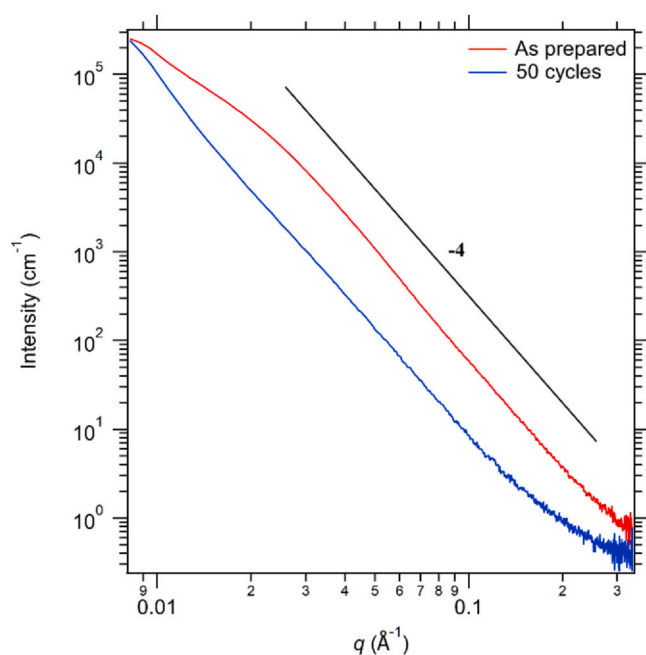

Fig. 7. SAXS data showing the Porod region (power law slope = −4) from where the specific surface area (SSA) was determined.

5. Conclusions

The combination of adding both ZrO_2 and Al_2O_3 to $CaCO_3$ has a positive effect as a cyclic stability of >80% is achieved at rapid calcination/carbonation times, *i.e.* 20 and 30 min, respectively. The reaction kinetics are fast, especially during carbonation. However, the calcination kinetics improve as the sample is cycled. The cyclic stability is hypothesised to arise from a synergetic effect of having both $CaZrO_3$ and Ca-Al-O compounds present in the sample, by preventing sintering of CaO/$CaCO_3$ particles and improving reaction kinetics, even better than the individual binary systems. This effect is highlighted by the larger specific surface area observed in the ternary system after cycling and the different morphology of the cycled material. However, the excessive presence of large zirconium-rich particles suggests that a smaller quantity of ZrO_2 may be sufficient in achieving the same benefits whilst lowering the overall price of the system. Furthermore, achieving a consistent cyclic stability comes at the expense of energy density, which for the Ca-Al-Zr system is theoretically 675 kJ kg^{-1} material compared to 1655 kJ kg^{-1} for pristine $CaCO_3$. However, the necessity for adding supporting materials to $CaCO_3$ seem inevitable if the material is to be enabled as an energy storage material. Finally, the energy density may not play a crucial role when it comes to bulk energy storage to support the electrical grid. This study suggests that combining different active properties of additives/catalysts may enhance the cyclic stability of a metal carbonate even further. The challenge is the selection of

Table 2
Comparison of the specific surface area between the binary systems $CaCO_3$-Al_2O_3(20 wt%) and $CaCO_3$-ZrO_2(40 wt%) and the ternary system $CaCO_3$-Al_2O_3(13.3 wt%)-ZrO_2(13.3 wt%).

Sample	Specific surface area (m^2 g^{-1})	# CO_2 cycles	Comments	Ref
$CaCO_3$-Al_2O_3 (20 wt%)	3.7(4)	0	As-milled	[23]
$CaCO_3$-Al_2O_3 (20 wt%)	1.2(1)	50	Absorbed	[23]
$CaCO_3$-ZrO_2 (40 wt%)	52(5)	0	As-milled	[23]
$CaCO_3$-ZrO_2 (40 wt%)	3.1(3)	50	Absorbed	[23]
$CaCO_3$-Al_2O_3(13.3 wt%)-ZrO_2(13.3 wt%)	50(5)	0	As-prepared	This work.
$CaCO_3$-Al_2O_3(13.3 wt%)-ZrO_2(13.3 wt%)	6(1)	50	Absorbed	This work.

additives based on price and properties and finding the minimum amount needed to maintain a cyclic stability. This opens up multiple new pathways for optimising the thermochemical energy storage properties of metal carbonates.

CRediT authorship contribution statement

Kasper T. Møller: Conceptualization, Formal analysis, Investigation, Writing – original draft, Visualization, Funding acquisition, Project administration, **Amanda Berger:** Investigation, **Mark Paskevicius:** Conceptualization, Formal analysis, Investigation, Writing – review & editing, Supervision, Funding acquisition, Project administration, **Craig E. Buckley:** Writing – review & editing, Funding acquisition.

Declaration of Competing Interest

The authors declare that they have no known competing financial interests or personal relationships that could have appeared to influence the work reported in this paper.

Acknowledgement

References

[1] M. Fellet, C.E. Buckley, M. Paskevicius, D.A. Sheppard, Research on metal hydrides revived for next-generation solutions to renewable energy storage, MRS Bull. 38 (2013) 1012–1013, https://doi.org/10.1557/mrs.2013.288

[2] D.N. Harries, M. Paskevicius, D.A. Sheppard, T.E.C. Price, C.E. Buckley, Concentrating solar thermal heat storage using metal hydrides, Proc. IEEE 100 (2012) 539–549, https://doi.org/10.1109/JPROC.2011.2158509

[3] A.J. Carrillo, J. González-Aguilar, M. Romero, J.M. Coronado, Solar energy on demand: a review on high temperature thermochemical heat storage systems and materials, Chem. Rev. 119 (2019) 4777–4816, https://doi.org/10.1021/acs.chemrev.8b00315

[4] T.D. Humphries, K.T. Møller, W.D.A. Rickard, M.V. Sofianos, S. Liu, C.E. Buckley, M. Paskevicius, Dolomite: a low cost thermochemical energy storage material, J. Mater. Chem. A 7 (2019) 1206–1215, https://doi.org/10.1039/C8TA07254J

[5] C. Ortiz, J.M. Valverde, R. Chacartegui, L.A. Perez-Maqueda, Carbonation of limestone derived CaO for thermochemical energy storage: from kinetics to process integration in concentrating solar plants, ACS Sustain. Chem. Eng. 6 (2018) 6404–6417, https://doi.org/10.1021/acssuschemeng.8b00199

[6] K.T. Møller, D. Sheppard, D.B. Ravnsbæk, C.E. Buckley, E. Akiba, H.-W. Li, T.R. Jensen, Complex metal hydrides for hydrogen, thermal and electrochemical energy storage, Energies 10 (2017) 1645, https://doi.org/10.3390/en10101645

[7] M. Hirscher, V.A. Yartys, M. Baricco, J. Bellosta von Colbe, D. Blanchard, R.C. Bowman, D.P. Broom, C.E. Buckley, F. Chang, P. Chen, Y.W. Cho, J.-C. Crivello, F. Cuevas, W.I.F. David, P.E. de Jongh, R.V. Denys, M. Dornheim, M. Felderhoff, Y. Filinchuk, G.E. Froudakis, D.M. Grant, E. Mac, A. Gray, B.C. Hauback, T. He, T.D. Humphries, T.R. Jensen, S. Kim, Y. Kojima, M. Latroche, H.-W. Li, M.V. Lototskyy, J.W. Makepeace, K.T. Møller, L. Naheed, P. Ngene, D. Noréus, M.M. Nygård, S. Orimo, M. Paskevicius, L. Pasquini, D.B. Ravnsbæk, M. Veronica Sofianos, T.J. Udovic, T. Vegge, G.S. Walker, C.J. Webb, C. Weidenthaler, C. Zlotea, Materials for hydrogen-based energy storage – past, recent progress and future outlook, J. Alloy. Compd. 827 (2020) 153548, https://doi.org/10.1016/j.jallcom.2019.153548

[8] L. André, S. Abanades, Recent advances in thermochemical energy storage via solid–gas reversible reactions at high temperature, Energies 13 (2020) 5859, https://doi.org/10.3390/en13225859

[9] G.S. Grasa, J.C. Abanades, CO2 capture capacity of CaO in long series of carbonation/calcination cycles, Ind. Eng. Chem. Res. 45 (2006) 8846–8851, https://doi.org/10.1021/ie0606946

[10] J.C. Abanades, D. Alvarez, Conversion limits in the reaction of CO2 with lime, Energy Fuels 17 (2003) 308–315, https://doi.org/10.1021/ef020152a

[11] F. Wang, T. Kuzuya, S. Hirai, J. Li, T. Li, Carbon dioxide absorption and release properties of pyrolysis products of dolomite calcined in vacuum atmosphere, Sci. World J. 2014 (2014) e862762, https://doi.org/10.1155/2014/862762

[12] S. Kumar, S.K. Saxena, A comparative study of CO2 sorption properties for different oxides, Mater. Renew. Sustain. Energy 3 (2014) 30, https://doi.org/10.1007/s40243-014-0030-9

[13] K. Zhang, X.S. Li, H. Chen, P. Singh, D.L. King, Molten salt promoting effect in double salt CO2 absorbents, J. Phys. Chem. C 120 (2016) 1089–1096, https://doi.org/10.1021/acs.jpcc.5b10729

[14] Q. Zhu, S. Zeng, Y. Yu, A model to stabilize CO2 uptake capacity during carbonation–calcination cycles and its case of CaO–MgO, Environ. Sci. Technol. 51 (2017) 552–559, https://doi.org/10.1021/acs.est.6b04100

[15] H. Takasu, J. Ryu, Y. Kato, Application of lithium orthosilicate for high-temperature thermochemical energy storage, Appl. Energy 193 (2017) 74–83, https://doi.org/10.1016/j.apenergy.2017.02.029

[16] K.T. Møller, K. Williamson, C.E. Buckley, M. Paskevicius, Thermochemical energy storage properties of a barium based reactive carbonate composite, J. Mater. Chem. A 8 (2020) 10935–10942, https://doi.org/10.1039/D0TA03671D

[17] C.-T. Yu, S.-Y. Chen, W.-C. Chen, P.-H. Chang, Method of fabricating high-temperature anti-sintering CO2 capture agent, US20150093317A1, (2015). ⟨https://patents.google.com/patent/US20150093317/en⟩ (Accessed March 18, 2019).

[18] C.-T. Yu, W.-C. Chen, Hydrothermal preparation of calcium–aluminum carbonate sorbent for high-temperature CO2 capture in fixed-bed reactor, Fuel 122 (2014) 179–185, https://doi.org/10.1016/j.fuel.2014.01.022

[19] L. Fedunik-Hofman, A. Bayon, S.W. Donne, Comparative kinetic analysis of CaCO3/CaO reaction system for energy storage and carbon capture, Appl. Sci. 9 (2019) 4601, https://doi.org/10.3390/app9214601

[20] N. Rong, Q. Wang, M. Fang, L. Cheng, Z. Luo, K. Cen, Steam hydration reactivation of CaO-based sorbent in cyclic carbonation/calcination for CO2 capture, Energy Fuels 27 (2013) 5332–5340, https://doi.org/10.1021/ef4007214

[21] Y.A. Criado, M. Alonso, J.C. Abanades, Kinetics of the CaO/Ca(OH)2 hydration/dehydration reaction for thermochemical energy storage applications, Ind. Eng. Chem. Res. 53 (2014) 12594–12601, https://doi.org/10.1021/ie404246p

[22] Outukumpu, HSC Chemistry, Houston, 1 edn, 2006, vol. 6.

[23] K.T. Møller, A. Ibrahim, C.E. Buckley, M. Paskevicius, Inexpensive thermochemical energy storage utilising additive enhanced limestone, J. Mater. Chem. A 8 (2020) 9646–9653, https://doi.org/10.1039/D0TA03080E

[24] D.A. Sheppard, M. Paskevicius, P. Javadian, I.J. Davies, C.E. Buckley, Methods for accurate high-temperature Sieverts-type hydrogen measurements of metal hydrides, J. Alloy. Compd. 787 (2019) 1225–1237, https://doi.org/10.1016/j.jallcom.2019.02.047

[25] K.S. Wallwork, B.J. Kennedy, D. Wang, The high resolution powder diffraction beamline for the Australian synchrotron, AIP Conf. Proc. 879 (2007) 879–882, https://doi.org/10.1063/1.2436201

[26] B. Schmitt, C. Brönnimann, E.F. Eikenberry, F. Gozzo, C. Hörmann, R. Horisberger, B. Patterson, Mythen detector system, Nucl. Instrum. Methods Phys. Res. Sect. Accel. Spectrom. Detect. Assoc. Equip. 501 (2003) 267–272, https://doi.org/10.1016/S0168-9002(02)02045-4

[27] B.R.S. Hansen, K.T. Møller, M. Paskevicius, A.-C. Dippel, P. Walter, C.J. Webb, C. Pistidda, N. Bergemann, M. Dornheim, T. Klassen, J.-E. Jørgensen, T.R. Jensen, In situ X-ray diffraction environments for high-pressure reactions, J. Appl. Crystallogr. 48 (2015) 1234–1241, https://doi.org/10.1107/S1600576715011735

[28] J. Hu, W. Cai, C. Li, Y. Gan, L. Chen, In situ x-ray diffraction study of the thermal expansion of silver nanoparticles in ambient air and vacuum, Appl. Phys. Lett. 86 (2005) 151915, https://doi.org/10.1063/1.1901803

[29] O. Spalla, S. Lyonnard, F. Testard, Analysis of the small-angle intensity scattered by a porous and granular medium, J. Appl. Crystallogr. 36 (2003) 338–347, https://doi.org/10.1107/S0021889803002279

[30] G. Beaucage, Approximations leading to a unified exponential/power-law approach to small-angle scattering, J. Appl. Crystallogr. 28 (1995) 717–728, https://doi.org/10.1107/S0021889895005292

[31] J. Ilavsky, P.R. Jemian, Irena: tool suite for modeling and analysis of small-angle scattering, J. Appl. Crystallogr. 42 (2009) 347–353, https://doi.org/10.1107/S0021889809002222

[32] A.M. Kierzkowska, R. Pacciani, C.R. Müller, CaO-based CO2 sorbents: from fundamentals to the development of new, highly effective materials, ChemSusChem 6 (2013) 1130–1148, https://doi.org/10.1002/cssc.201300178

[33] J.R. Salasin, S.E.A. Schwerzler, R. Mukherjee, D.J. Keffer, K.E. Sickafus, C.J. Rawn, Direct formation and structural characterization of electride C12A7, Materials 12 (2019) 84, https://doi.org/10.3390/ma12010084

[34] Kasper T. Møller Terry D. Humphries Amanda Berger Mark Paskevicius Craig E. Buckley Chemical Engineering Journal Advances doi: 10.1016/j.ceja.2021.100168. In press.